https://doi.org/10.5194/se-2019-203
Preprint. Discussion started: 24 February 2020
© Author(s) 2020. CC BY 4.0 License.

Solid Earth Discussions

Increased LLVP density recovered by seismologically constrained gravity inversion

Wolfgang Szwillus[1], Jörg Ebbing[1], and Bernhard Steinberger[2]

[1]Institut für Geowissenschaften, Christian-Albrechts-Universität zu Kiel
[2]Geoforschungszentrum Potsdam

Correspondence: Wolfgang Szwillus (wolfgang.szwillus@ifg.uni-kiel.de)

1 Abstract

The nature and origin of the two Large Low Velocity Provinces in the lowest part of the mantle remain controversial. They have been interpreted as a purely thermal feature, accumulation of subducted oceanic lithosphere or a primordial zone of iron enrichment. Information regarding the density of the LLVPs would help to constrain a possible explanation.

In this work, we perform a density inversion for the entire mantle, by constraining the geometry of potential density anomalies using tomographic vote maps. Vote maps describe the geometry of potential density anomalies according to their agreement of multiple seismic tomographies, hence not depending on a single representation. Therefore, the geometries used for inversion are features observed in most tomographies. We use linear inversion and determine the regularization parameters using cross-validation. Two different input fields are used to study the sensitivity of the mantle density results to the treatment of the lithosphere. We find the best data fit is achieved if we assume that the lithosphere is in isostatic balance.

The estimated densities obtained for the LLVPs are systematically positive density anomalies for the LLVPs in the lower 800-1000 km of the mantle, which would indicate a chemical component for the origin of the LLVPs. Both iron-enrichment and a MORB contribution are in accordance with our data, but the required super-adiabatic temperature anomalies for MORB would be close to 1000 K.

2 Introduction

Seismology has systematically revealed more and more of the heterogeneity in the mantle. Interpretations of seismic images often aim at determining the density of features, because buoyancy is the driver of mantle dynamics. For instance, much research has focused on tracing sinking slabs in order to understand how subduction functions (e.g. van der Meer et al. (2018)). At greater depths such interpretation becomes more difficult, due to reduced resolution and lack of corroborating surface evidence. The most striking feature of the lowermost mantle are probably the Large Low Velocity Provinces (LLVPs) (Garnero et al., 2016).

The two LLVPs are antipodal regions of decreased seismic velocity that extend from the core-mantle boundary about 400-800 km into the mantle and cover about 25 % of the surface of the core-mantle boundary (Garnero et al., 2016). There is

https://doi.org/10.5194/se-2019-203
Preprint. Discussion started: 24 February 2020
© Author(s) 2020. CC BY 4.0 License.


considerable debate regarding their nature and origin, either interpreted as a purely thermal feature (Koelemeijer et al., 2017), an accumulation of subducted oceanic lithosphere (Mulyukova et al., 2015) or iron-enriched zones (Ballmer et al., 2015; Deschamps et al., 2012). In addition, the margins of the LLVPs have been considered tectonically stable Plume Generation Zone (PGZ), because Large Igneous Provinces and Kimberlites concentrate along their margins (Burke et al., 2008; Conrad et al., 2013).

The debate regarding the LLVPs is often centered on their density, because density allows to distinguish between a purely thermal and a thermo-chemical origin. However, direct determinations of density using seismological and geodetic methods have led to contradictory results, sometimes indicating positive (Ishii and Tromp, 1999; Lau et al., 2017; Moulik and Ekström, 2016) and negative densities (Koelemeijer et al., 2017), with a strength between 0.5 % and 2.0 %.

Combining seismology and gravity to investigate the mantle is a well-established approach that typically includes dynamical modelling of mantle convection (Richards and Hager, 1984; Hager and O'Connell, 1979). Most commonly, seismic velocities are directly converted into densities and the vertical viscosity distribution is adjusted in order to fit the geoid (Richards and Hager, 1984). Using this technique, many models of viscosity and density inside the mantle have been derived (King, 1995, 2016; Steinberger, 2007, 2016; Richards and Hager, 1984; Hager et al., 1985).

While viscosity inversions can successfully explain the geoid with variance reductions of 80 % or more (King and Masters, 1992; Ricard et al., 1993), this approach relies on some assumptions that can be challenged. Linearly converting seismic velocity anomalies into density anomalies implies a purely thermal origin (Karato, 1993). However, differences in terms of composition certainly play a role in the upper mantle/lithosphere (Griffin et al., 2009) and have been suggested for the lower mantle as well (Ballmer et al., 2017; Deschamps et al., 2012).

Furthermore, the modelled geoid associated with a certain density distribution is partly based on the dynamic topography caused by this density distribution. Thus, viscosity inversion should also reproduce surface topography, since it is an important part of the total gravity effect. However, before the dynamic predictions can be compared to real topography, the isostatic part of topography must be removed using crustal models. While the agreement between predicted and non-isotatic models has been increasing (Flament et al., 2013; Steinberger, 2016), there are still considerable differences (Molnar et al., 2015).

In this contribution, we explore an alternative approach for fitting the gravity field using mantle density structure. Instead of density-velocity conversion, we use tomographic vote maps (Lekic et al., 2012; Shephard et al., 2017) to provide geometrical constraints for a linear gravity inversion. The geometry is defined by the fast and slow zone derived from the vote maps and each zone is assigned an unknown but constant density. These densities are completely free parameters that are adjusted to fit the gravity field. As input data we use satellite gravity data, corrected for topography and lithosphere. For the latter correction we compare two different approaches. In the first approach it is assumed that the lithosphere is in perfect isostatic balance and in the second we make use of a recently developed crustal model by us (Szwillus et al., 2019).

The justification for directly inverting density instead of going through viscosity is that the gravity field is only affected indirectly by the viscosity distribution, through viscosity's influence on the deformation of the boundaries (surface and core-mantle boundary) (Hager and O'Connell, 1979). However, the gravity effect of any deformed boundary is independent of what caused the deformation. Thus, the gravity effect of the top boundary (i.e. topography) can simply be calculated and removed

https://doi.org/10.5194/se-2019-203
Preprint. Discussion started: 24 February 2020
© Author(s) 2020. CC BY 4.0 License.

from the observed data, without needing any dynamic simulations or viscosity structures. In contrast, there are few compatible direct observations of core-mantle boundary deformation and hence it cannot be accounted for a priori (e.g. Tanaka (2010)). However, CMB deformation is mostly related to density anomalies below 2000 km depths (kernels in e.g. Colli et al. (2016)). At these depths, it does not make a great difference, whether a density anomaly is balanced isostatically on the CMB or dynamically. Hence, the gravity response of a mass anomaly and its (isostatic) compensation at the CMB have very similar wavelengths content and the gravity anomalies are simply weakened by the isostatic CMB deformation, but not changed in shape. Furthermore, the composition, structure and dynamic behaviour of the outer layers of the core might be very complex and it is unclear how the outer core is coupled to the lower mantle (Mound and Buffett, 2003; Roberts and Aurnou, 2012).

3 Methods and data

3.1 Gravity data

We use satellite gravity data from the global gravity field model GOCO05S (Pail et al., 2010) at the measurement height (225 km) of the GOCE satellite in its last mission phase (van der Meijde et al., 2015). This way, we stay close to the original source of the data and avoid any issues related to omission error (Bouman et al., 2013).

As a first step we calculate an ice-corrected Bouguer anomaly based on the topography of ETOPO1 (Amante and Eakins). Onshore we assume a density of 2670 $\mathrm{kg\,m^{-3}}$, and offshore we use a correction density of 1770 $\mathrm{kg\,m^{-3}}$ based on a reference crustal density of 2800 $\mathrm{kg\,m^{-3}}$ and a water density of 1030 $\mathrm{kg\,m^{-3}}$. In addition, the influence of ice is removed assuming a density of 917 $\mathrm{kg\,m^{-3}}$.

Since we are interested in the mantle density structure, the second step is to account for the gravity effect of the crust and/or lithosphere. Two inherently different approaches exist to achieve this. The first option is to assume some form of isostatic compensation and use this to account for the crust and/or lithosphere. Alternatively, the gravity effect of crustal models, such as Crust1.0 (Laske et al., 2013) or Litho1.0 (Pasyanos et al., 2014) can be calculated. While the latter approach includes more geophysical data, it also 'propagates' any errors of the crustal model into the mantle. In particular, all crustal models predict several kilometers of residual topography, even in the continents (Steinberger, 2016) and are thus not nearly in isostatic balance. As a consequence, the topography would need to be supported dynamically, which should lead to much higher free-air anomaly values (Molnar et al., 2015).

In light of this discrepancy, we explore two approaches. In the first approach, we assume that continental topography is compensated by crustal thickness variations, whereas ocean floor depth is compensated by variations of the mantle lithosphere density (the same isostatic model as in Szwillus et al. (2016)). The *isostatic residual* is then:

$$\mathrm{Isostatic\,residual} = \mathrm{FA} - g_{\mathrm{topo}} - g_{\mathrm{iso}}. \tag{1}$$

Where FA is the free-air anomaly (Fig. 1a), g_{topo} is the gravity effect of topography and g_{iso} is the gravity effect of the isostatic compensation masses.

https://doi.org/10.5194/se-2019-203
Preprint. Discussion started: 24 February 2020
© Author(s) 2020. CC BY 4.0 License.

Solid Earth Discussions

In the second approach, we use our recent crustal model based on kriging (Szwillus et al., 2019) and assume a density contrast between crust and mantle of 400 $\mathrm{kg\,m^{-3}}$ to estimate the gravity effect of varying crustal thickness. This gives the *crustal residual*:

$$\mathrm{Crustal\,residual} = \mathrm{FA} - g_{\mathrm{topo}} - g_{\mathrm{crust}}. \tag{2}$$

Where, g_{crust} is the gravity response of the crustal thickness variations.

The isostatic residual is very similar to the free-air anomaly (Fig. 1b), except in areas of high topography. In contrast, the crustal residual has a much higher amplitudes and patterns (Fig. 1c). For comparison we also computed the residual (non-isostatic) topography of the kriging crustal model (Szwillus et al., 2019), which anti-correlates with the crustal residual on large scales (Fig. 1d).

3.2 Geometry constraints

Additional constraints are required to overcome the inherent non-uniqueness of a density inversion. We use information from whole mantle seismic tomographies in the form of vote maps (Shephard et al., 2017) to define volumes which could potentially contain density anomalies. Vote maps were first introduced by Lekic et al. (2012) in the context of cluster analysis and then further developed by Shephard et al. (2017). A vote map is based on a collection of tomography models and at each point it gives the number of tomographies that detect a significant anomaly at that location. The threshold what constitutes a significant anomaly is the standard deviation at that depth for each seismic tomography. Thus, even tomographies with vastly different amplitude ranges can be combined in a single vote map. We used the vote maps based on 17 S-wave tomography models as available on SubMachine (Hosseini et al., 2018) at a resolution of 1 degree and 100 km depth spacing. There are two separate vote maps for positive and negative anomalies. Fig. 2 shows an example of the vote maps at depth of 2700 km, close to the core-mantle boundary.

The first step is to discretize the inversion problem by extracting regions of potential density anomalies from the vote map individually for each depth. Our underlying assumption is that density anomalies only occur in horizontally connected regions where at least N tomographies detect anomalous velocity. We choose $N = 10$, because this is the cut-off that correlates with the strongest gradients of the vote maps. Each connected region is assigned a constant but unknown density. As a result of this process, we have a total of 1135 anomalous regions that is each described in terms of its depths, its pixels and an unknown density value. These density anomalies are completely free parameters that will be adjusted during the inversion to fit the gravity field. Importantly, we impose no correlation between velocity and density.

3.3 Cross-validation inversion approach

Our inversion is a two-step approach. First, we forward calculate for each potential density anomaly region its characteristic gravity response. Second, the characteristic gravity responses of all of the potential density anomalies are placed into a design matrix $\mathbf{A}$ and solved with a generalized Tikhonov regularization technique. The regularization parameters are chosen based on cross-validation.

https://doi.org/10.5194/se-2019-203
Preprint. Discussion started: 24 February 2020
© Author(s) 2020. CC BY 4.0 License.

Solid Earth
Discussions
Open Access
EGU

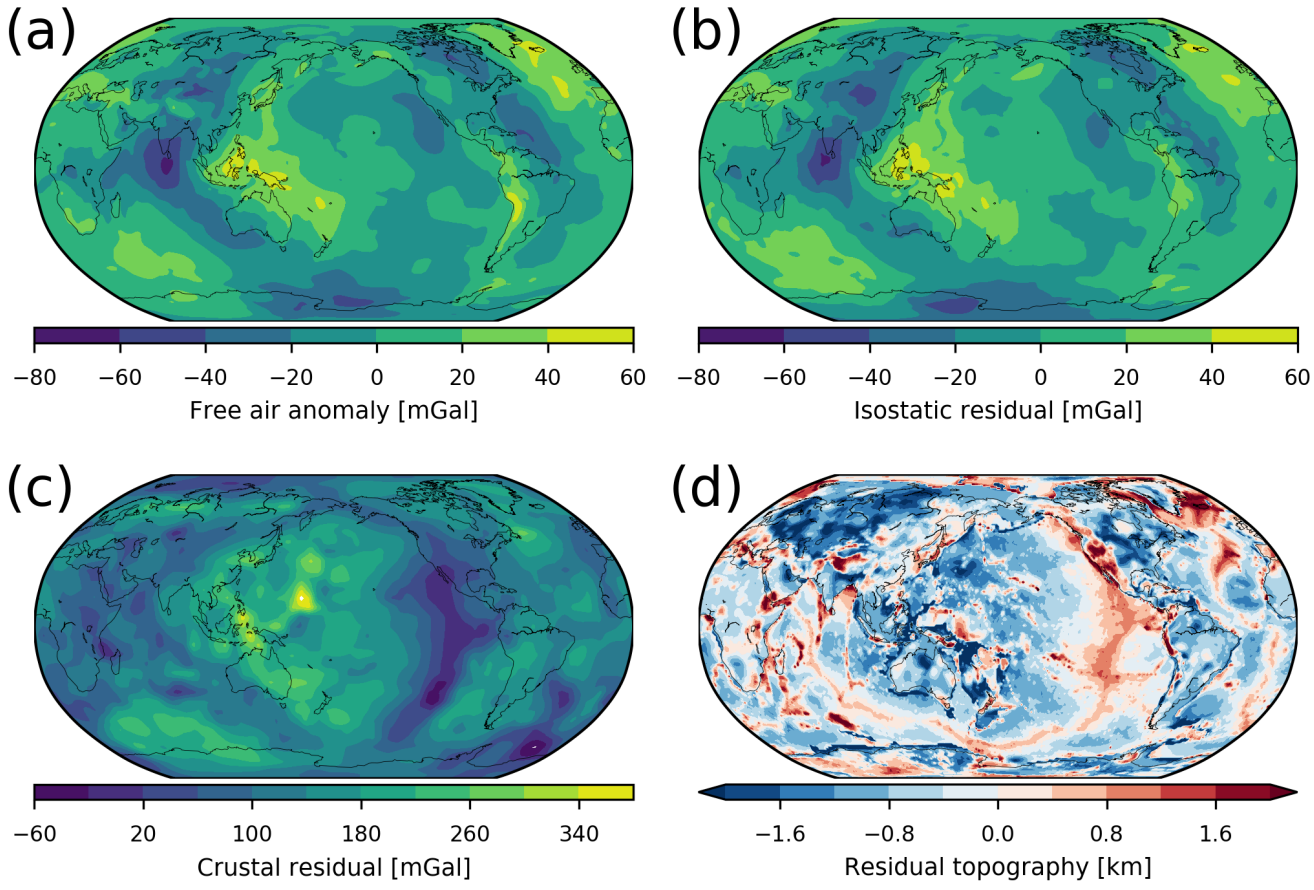

Figure 1. Input data for the inversions. a) Free-air anomaly at a measurement height of 225 km. b) Isostatic residual gravity anomaly at 225 km height. This is obtained by correcting for the presence of topography and isostatic compensation masses. c) Crustal residual gravity anomaly at 225 km height obtained by removing the gravity effect of the crustal model. d) Residual topography after removing the isostatic contribution of the crustal model.

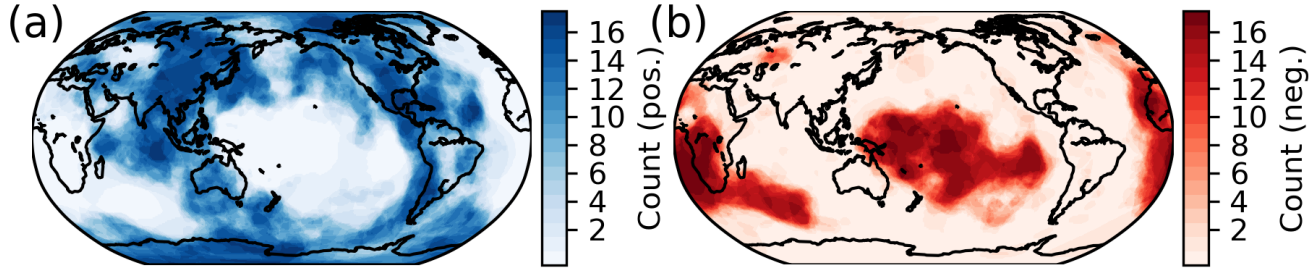

Figure 2. Votemaps at 2700 km depths. a) Vote map for fast (positive) anomalies, b) Vote map for slow (negative) anomalies. Note the clear signature of the two LLVPs underneath Africa and Central Pacific.

https://doi.org/10.5194/se-2019-203
Preprint. Discussion started: 24 February 2020
© Author(s) 2020. CC BY 4.0 License.

Solid Earth Discussions

The forward response is calculated by placing a point mass with a constant density of 1 at each pixel of the potential density anomaly with a volume V, given by:

$$V = r^2 \cos(\mathrm{lat})(\Delta\phi)^2 \Delta z, \tag{3}$$

where r is the radius, lat is the latitude, $\Delta\phi$ is the angular size of each mass (1 degree) and Δz is the vertical resolution (100 km). The gravity caused by each point mass at a location (r,lat,lon) is given by:

$$g(r_s, \mathrm{lat}_s, \mathrm{lon}_s) = Gm \frac{r_s - r\cos\gamma}{(r^2 + r_s^2 - 2rr_s\cos\gamma)^{3/2}}, \tag{4}$$

where γ is the great-circle distance between the location and the point mass and $G = 6.67428 \cdot 10^{-11} \frac{\mathrm{m}^3}{\mathrm{kg\,s}^{-2}}$ is the gravitational constant. The total gravity effect of each potential density anomaly is then found by summing over the gravity effect of all pixels.

Next, the gravity response of all of the potential density anomalies are placed into the design matrix $\mathbf{A}$, where A_{ij} is the gravity effect of potential density anomaly j on measurement point i. In principle, the density values associated with each anomaly are found as $\mathbf{A}^{-1}\mathbf{g}$, where $\mathbf{g}$ contains all of the gravity values. However, in practice the solution will be unstable and non-unique, so that regularization is required. Here, we choose to minimize the following least-squares functional:

$$\chi(\rho)^2 = ||\mathbf{A}\rho - \mathbf{g}||^2_{\Sigma_g^{-1}} + \beta||\rho||^2 + \gamma||\mathbf{D}\rho||^2. \tag{5}$$

The three terms relate to the data misfit, the magnitude of density variations and the vertical derivative of density. $||\cdot||_M$ is the quadratic form related to matrix M, and $||\cdot|| = ||\cdot||_I$ is the euclidean norm. β and γ are the regularization parameters that enforce minimization of absolute norm of the density values and the vertical derivative of the density respectively. In addition, the parameter β represents the ratio of data variance to model variance. $\mathbf{D}$ is a finite differencing matrix consisting of first order forward vertical differences of density. Finally, Matrix Σ_g is an assumed correlation matrix of the gravity values. We use an isotropic correlation function with a correlation distance of 10 degrees, based on a semi-variogram analysis (Chilès and Delfiner, 2012). The main purpose of the matrix is to down-weigh observation points near the pole, which are otherwise over represented due to convergence near the pole.

The optimal ρ belonging to this formulation is:

$$\hat{\rho} = \left(\mathbf{A}^T\Sigma_g^{-1}\mathbf{A} + \beta I + \gamma D^T D\right)^{-1} \mathbf{A}^T\Sigma_g^{-1}\mathbf{g}. \tag{6}$$

The regularization parameters β and γ exert critical control over the resulting density structure and the achievable data fit. Unfortunately, choosing regularization parameters is often ad-hoc (for example L-curves), which limits the significance of the results. A somewhat more robust way to determine regularization parameters is cross-validation (Efron and Gong, 1983).

In k-fold cross validation, the gravity data set is randomly split into k distinct index sets $\mathcal{I}_j$. The first set $\mathcal{I}_\infty = \mathcal{T}$ then becomes the **training set** and the remaining sets are combined to form the **validation set** $\mathcal{V}$. The training set is then used to solve the inversion problem giving a solution ρ_1. Based on how well ρ_1 predicts the data in $\mathcal{T}$ and $\mathcal{V}$, the training and validation misfit is calculated. Each $\mathcal{I}_|$ becomes the training set once and this repeated for many random partitions of the data.

https://doi.org/10.5194/se-2019-203
Preprint. Discussion started: 24 February 2020
© Author(s) 2020. CC BY 4.0 License.

Solid Earth Discussions

By design, the training misfit is minimal when β and γ are zero (if there are no numerical instabilities). However, small values of β and γ also risk over-fitting the data. By carrying out cross-validation for all combinations of β and γ in a reasonable range of values, the optimal β and γ corresponding to the minimum validation misfit can be found.

Apart from constraining the regularization parameters, this procedure also gives a bootstrap estimate (Efron and Gong, 1983) of the density structure. The collection of all the density estimates derived for all subsets of gravity data can be used to calculate a mean density value and its standard deviation for each potential anomaly, given certain regularization parameters. This is useful to determine how robust a single density anomaly is.

3.4 Boundary topography

The surface and CMB deformations implied by the density model recovered by inversion is important to judge the quality of the results. The surface topography predicted by the density model should roughly agree with the residual topography, because topography is strongly sensitive to density. The magnitude of the CMB deformation is required to assess how much they affect the gravity field fitting.

We determine the deformation of the upper and lower domain boundary caused by density structure as a post-processing step after inversion. We use both an isostatic and a dynamic formulation to determine this deformation.

Let $t_{CMB}(\mathrm{lat}, \mathrm{lon})$ be the CMB-topography as a function of longitude and latitude. Under the assumption of isostatic balance at the CMB, we find:

$$t_{CMB}(\mathrm{lat}, \mathrm{lon}) = -\frac{1}{\Delta\rho_{CMB}} \int_{CMB}^{CMB+H} \delta\rho(r, \mathrm{lat}, \mathrm{lon})\, \mathrm{d}r.$$

Where $\Delta\rho_{CMB}$ is the density jump at the CMB, H is the height above the CMB where isostatic balance applies and $\overline{\rho}$ is the mean density between $r = CMB$ and $r = CMB + H$.

We convert the density difference associated with undulating topography into a surface density $\sigma = t_{CMB}\Delta\rho_{CMB}$ and calculate its gravity response in spherical harmonics by:

$$g = \sum_{l,m} g_l^m Y_l^m = \sum_{l,m} 4\pi G \frac{l+1}{2l+1} \left(\frac{r_{CMB}}{r_s}\right)^{l+2} \sigma_l^m Y_l^m,$$

where σ_l^m are the spherical harmonic coefficients of the surface density, Y_l^m is a spherical harmonic function and $r_s = 6371 + 225\,\mathrm{km}$ is the radius of the observations.

Isostatic surface topography is calculated in the same way using the upper 300 km of the domain and a density contrast of 2670 kgm^{-3} at the surface.

To determine the dynamic surface and CMB topography we use the propagator matrix approach of Hager and O'Connell (Hager and O'Connell (1979)), assuming a two-layer mantle viscosity structure, consisting of low viscosity between 0-700 km and high viscosity below 700 km depth. Free slip boundary conditions are assumed on the surface and CMB. The resulting kernels show that for a layered viscosity structure, the influence of density anomalies below 500 km is limited for topography, even at very long wavelengths (Fig. 3a). The CMB kernels decrease much more slowly, even with a layered viscosity (Fig. 3b)

https://doi.org/10.5194/se-2019-203
Preprint. Discussion started: 24 February 2020
© Author(s) 2020. CC BY 4.0 License.

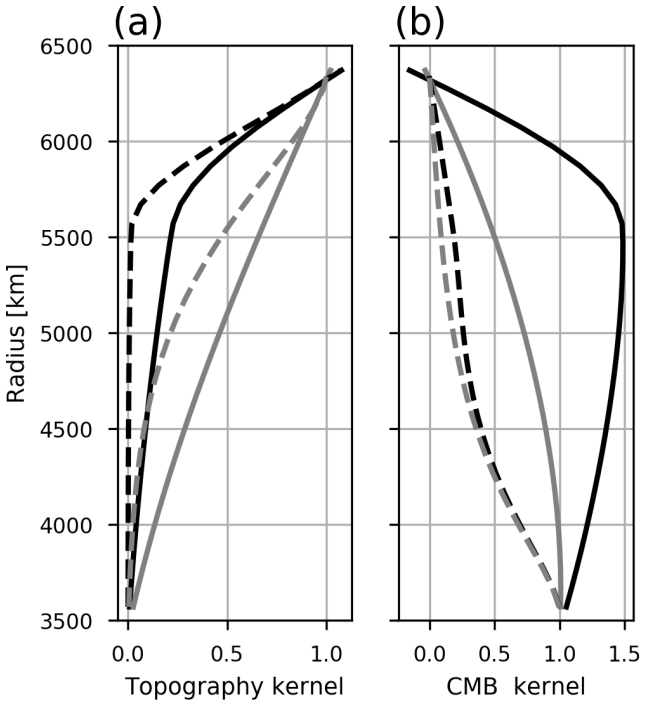

Figure 3. Topgoraphy and CMB kernels calculated using the propagator matrix approach (Hager and O'Connell, 1979). The black line is computed using a two-layer viscosity structure, the grey line uses a constant viscosity. The solid line is for spherical harmonic degree 2 and the dashed line for spherical harmonic degree 10.

and even at degree 10.

4 Results

4.1 Inversion using isostatic residual

A grid-search of β and γ values between 10^{-3} and 10^{3} using the cross-validation procedure leads to a minimum validation misfit of 5.32 mGal if $\beta = 0.03$ and $\gamma = 1.0$ (Fig. 4a). Although this minimum is not particularly well developed, we proceed with these values of β and γ, since neighboring regularization settings give similar results. With these regularization parameters, the training misfit becomes 3.25 mGal, which is about 20 % of the RMS of the input gravity field (96% variance reduction).

The inversion is able to reasonably reproduce the main features of the isostatic residual gravity field (Fig. 4b). However, the amplitude of the residual field is systematically too small. A linear regression of the gravity field predicted from the model

https://doi.org/10.5194/se-2019-203
Preprint. Discussion started: 24 February 2020
© Author(s) 2020. CC BY 4.0 License.

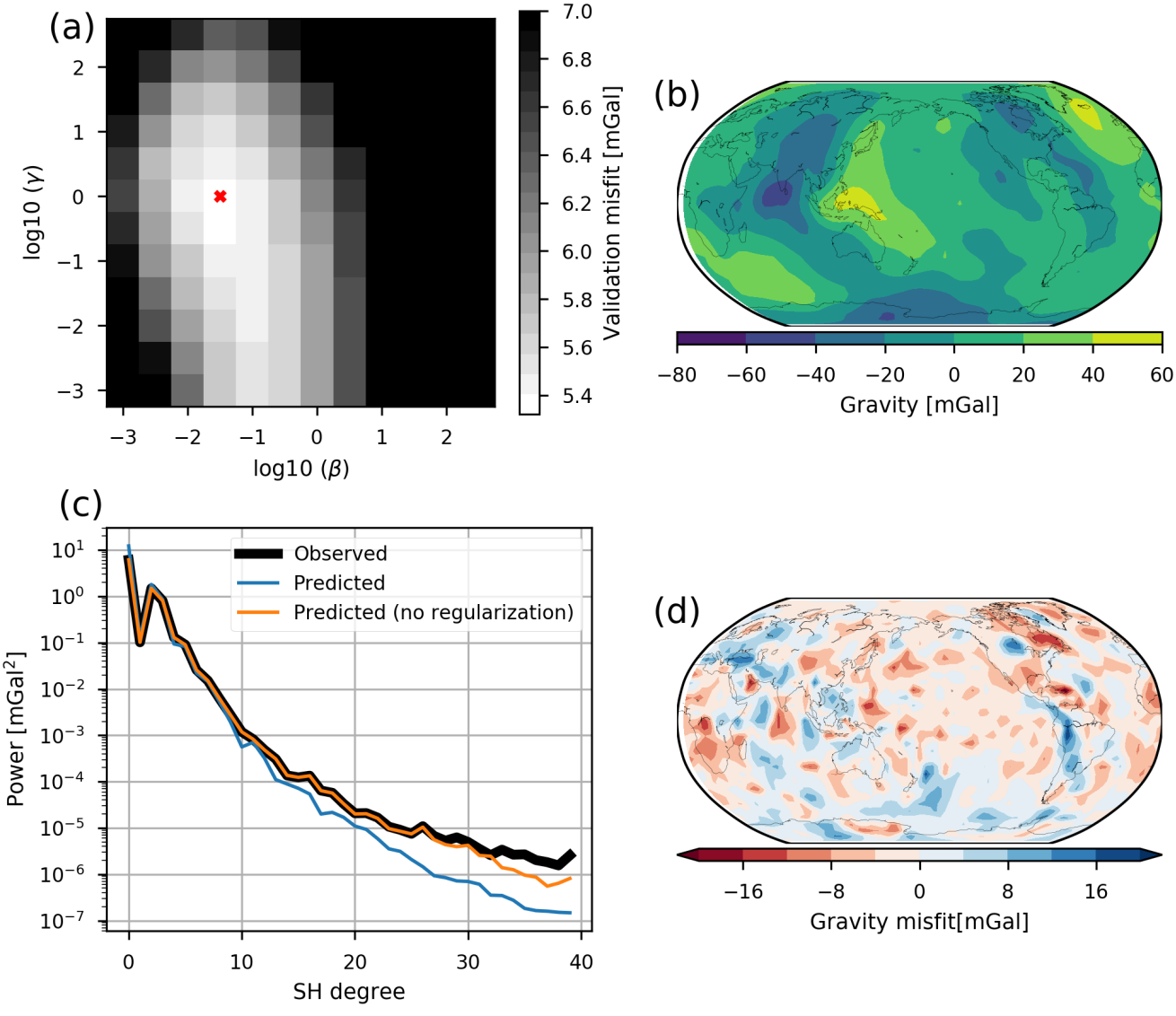

Figure 4. Results of the inversion using the isostatic residual. a) Validation misfit as a function of regularization parameter β. b) Predicted field of the inversion results. c) Spectral comparison of the input and predicted data. d) Difference between input and predicted data.

https://doi.org/10.5194/se-2019-203
Preprint. Discussion started: 24 February 2020
© Author(s) 2020. CC BY 4.0 License.

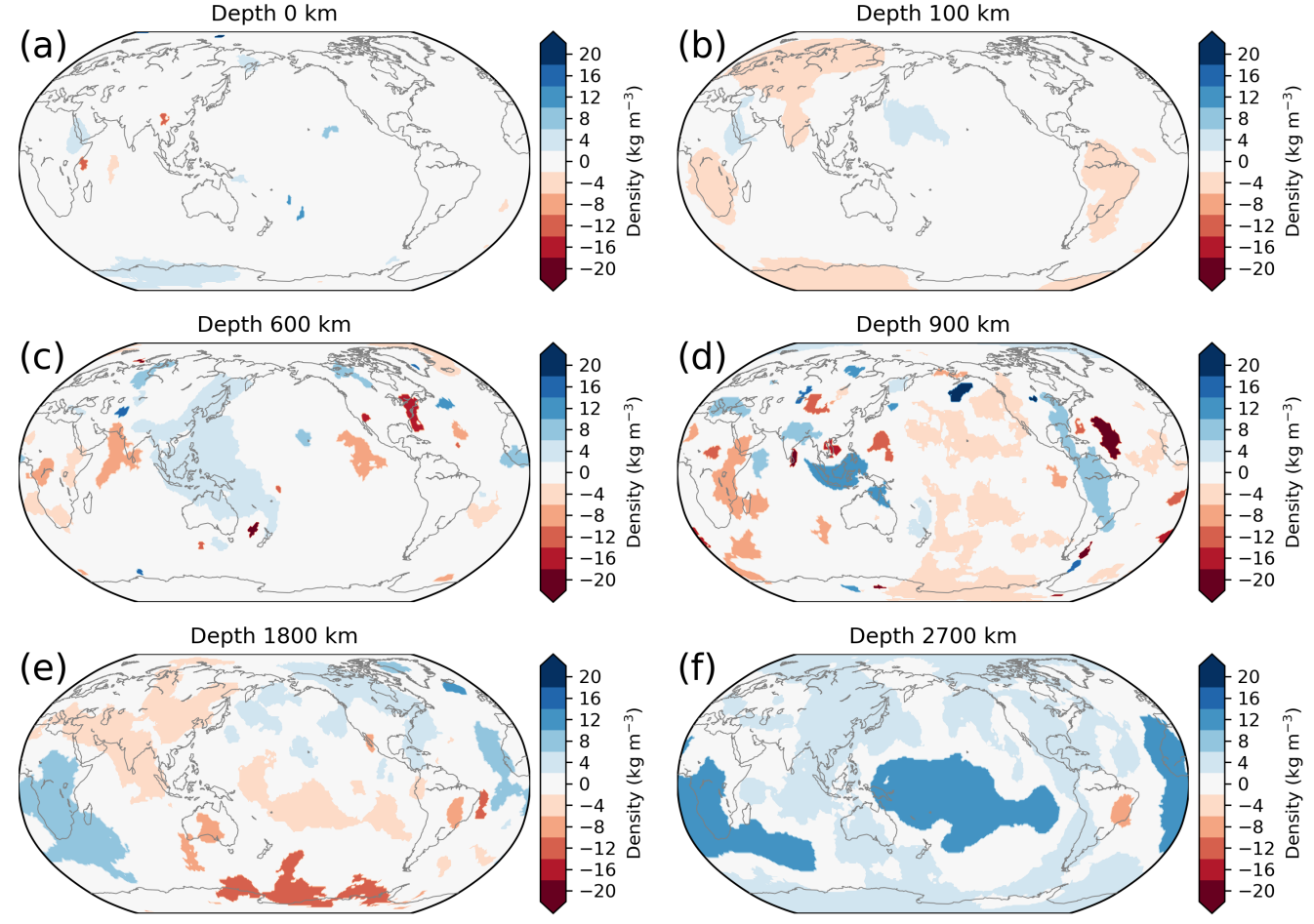

Figure 5. Density slices through selected depths of the inversion results using the isostatic residual.

against the measured values gives a linear factor of 0.85, implying that the modelled anomalies are about 15 % too weak. This is probably a result of the regularization.

In spectral domain, the predicted gravity field is able to reproduce the long-wavelength part up to spherical harmonic degree 10 (Fig. 4c). At shorter wavelengths, the predicted field is systematically too weak, going down to less than 10 % of the observed data at spherical harmonic degree 40. For comparison, the solution with no regularization ($\beta = \gamma = 0$) is able to reproduce the spectrum up to spherical harmonic degree 25 perfectly. Thus, wavelengths shorter than SH degree 25 simply cannot be produced, due to the insufficient spectral content of the vote maps.

The inverted density anomalies show no correlation with sign of the velocity anomaly, which would suggest that many density anomalies are not caused only by temperature variations. The spatial distribution is highly complex and not all density anomalies are easily related to expected features. However, some first-order trends can be identified (Fig. 5).

https://doi.org/10.5194/se-2019-203
Preprint. Discussion started: 24 February 2020
© Author(s) 2020. CC BY 4.0 License.

Solid Earth Discussions

The upper 100 km of the inversion results contain very little density variations (5a). Some cratons (South America, South Africa, Eurasia) show a slight negative density anomaly (5b). This likely related to simplifications in our isostatic model and not representative of the actual density structure

At greater depths, subducted slabs would be expected in the density structure. This is overall reflected in our density inversion results, but not all slabs are resolved as positive density anomalies over their complete depth range. For example, the Andean slabs can be seen at depths at a depth of 900 km depth as an anomaly of +6 $\mathrm{kg\,m^{-3}}$ (5d), but not at 600 km depth.

The LLVPs have systematically a positive density of up to +10 $\mathrm{kg\,m^{-3}}$ (5e and f). The top of the African LLVP appears at a depth of 1800 km depth and extends down to the CMB. The Pacific LLVP only appears at greater depths of 2200 km and is also continuous to the CMB. Both LLVPs are overlain by slight negative density anomalies.

4.2 Inversion using crustal residual

The preferred regularization parameters derived by the cross-validation procedure are the similar as for the isostatic residual, $\beta = 0.1$ and $\gamma = 1.0$ (Fig. 6a). With these values, a validation misfit of 34 mGal and a training misfit of 23 mGal is achieved, which corresponds to about 40 % of the input signal. Thus, the fit for the crustal residual is considerably worse than for the isostatic residual, both in an absolute and a relative sense. The predicted and input gravity data only agree qualitatively in some areas (Fig. 6b), and large residuals remain (Fig. 6d).

Overall the inverted density variations are much larger for the crustal residual than for the isostatic residual (Fig. 7). In the upper 300 km or so, this is expected, since the lithospheric density structure has not been accounted for by the crustal model. The ocean cooling trend is not imaged well by the vote maps and as a result, only the Pacific and Indian Ocean spreading ridges are resolved as crude negative density anomalies (Fig. 7a) . Some cratons (North America, Eurasian) show strong positive density anomalies ($30 \frac{\mathrm{kg}}{\mathrm{m^3}}$), but this is neither consistent vertically nor applies to most geographical regions (Fig. 7a and b). Thus, the ability to resolve mantle lithospheric sources is limited and probably contributes to the poor fit of the data.

At 600 and 900 km depth some subduction-related density anomalies can be seen, but overall correlation is poor. Only in the lowest mantle a more consistent picture emerges, in particular the LLVPs are resolved as positive density anomalies (+40 $\mathrm{kg\,m^{-3}}$). As in the case with isostatic residual, the African LLVP appears to extend further upwards as a positive density anomaly than the Pacific LLVP (Fig. 7e and f).

5 Discussion

5.1 Resolved mantle structure

While the main features observed are the LLVPs, it is important to also scrutinize the results for the remaining mantle. A long-wavelength error in the upper mantle density structures leads to an incorrect estimate of the density of the LLVPs . In the upper mantle above the transition zone (410 - 670 km depth) much of the seismic image can be linked to tectonic features: Thick and cold lithospheric roots underlie the cratonic cores of the continents and can extend up to 300 km deep (Schaeffer and

https://doi.org/10.5194/se-2019-203
Preprint. Discussion started: 24 February 2020
© Author(s) 2020. CC BY 4.0 License.

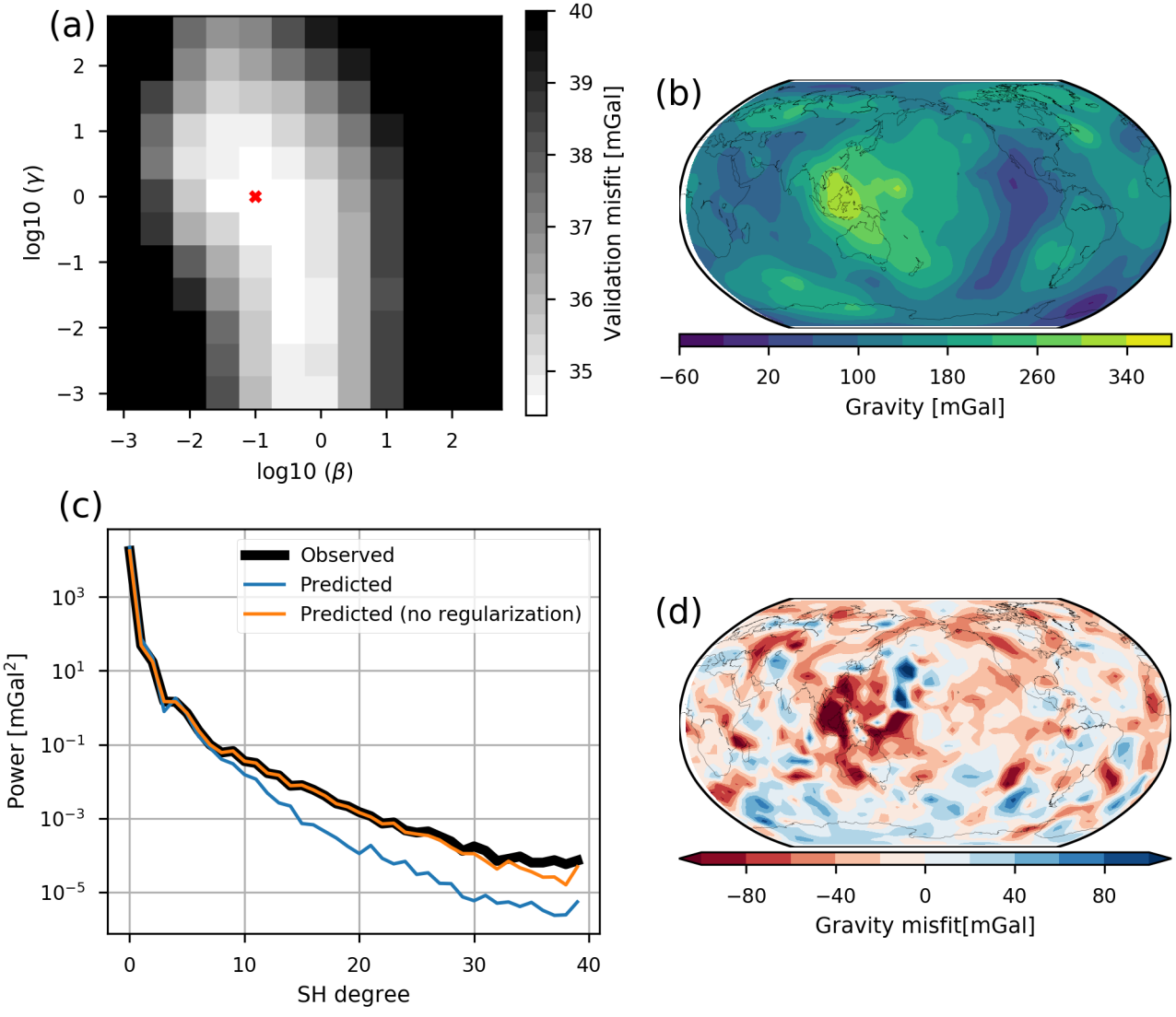

Figure 6. Results of the inversion using the crustal residual. a) Validation misfit as a function of regularization parameter β. b) Predicted field of the inversion results. c) Spectral comparison of the input and predicted data. d) Difference between input and predicted data.

https://doi.org/10.5194/se-2019-203
Preprint. Discussion started: 24 February 2020
© Author(s) 2020. CC BY 4.0 License.

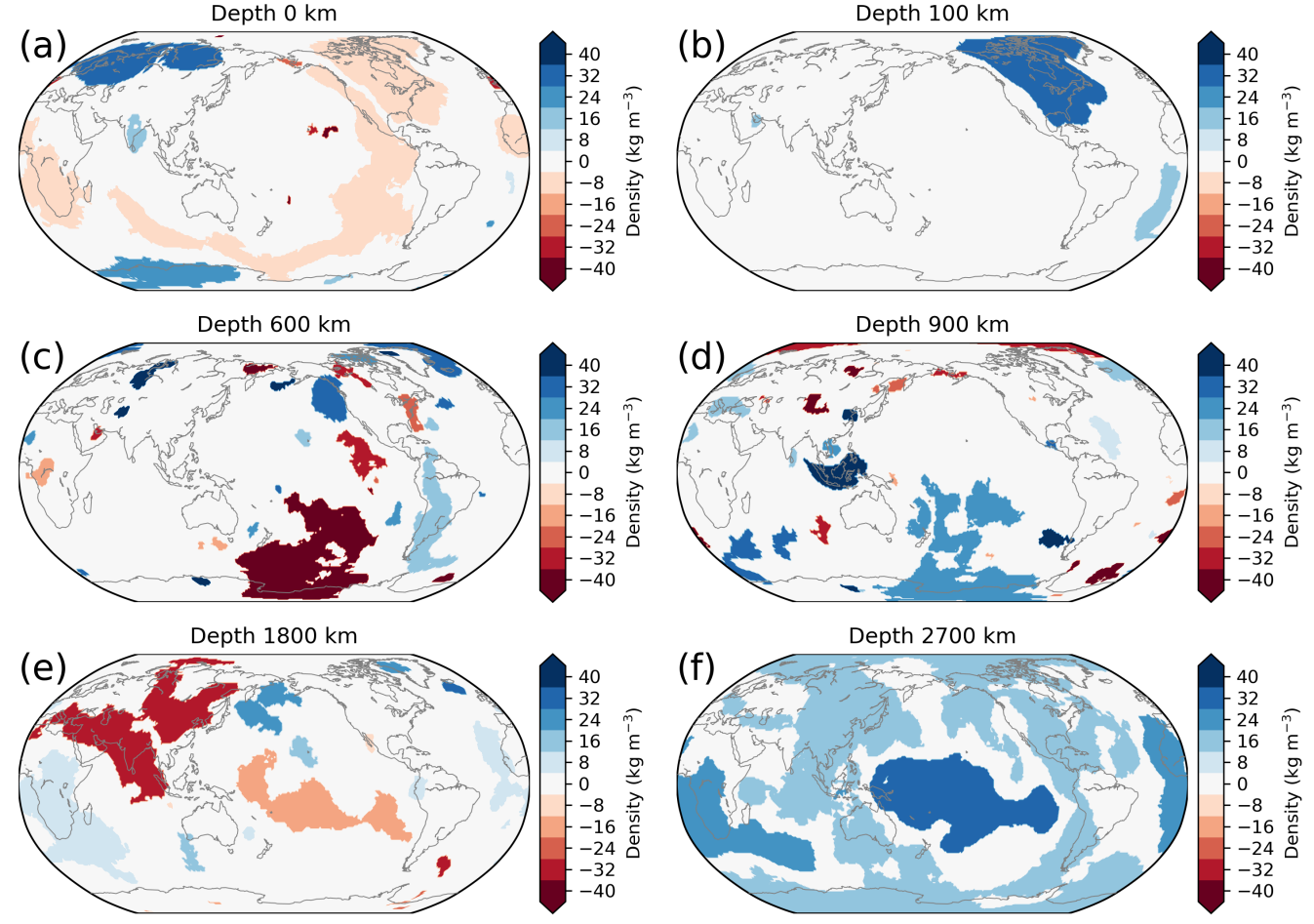

Figure 7. Density slices through selected depths of the inversion results using the crustal residual.

Lebedev, 2015), the oceans are characterized by a velocity trend related to cooling of the lithosphere (Priestly and McKenzie, 2006) and slabs formed during subduction sink through the mantle, sometimes stagnating at various depths and sometimes passing through the transition zone to the lowermost mantle (e.g. van der Meer et al. (2018)).

The cratonic lithospheric mantle density is the result of a complex interaction between temperature, composition and mineralogy (Griffin et al., 2009; Fullea et al., 2009; Afonso et al., 2013). The density increase due to low temperature is probably (partially) offset by its depleted composition (the isopycnic hypothesis Jordan (1978)). Indeed, a slightly increased density (+5 to 7.5) is recovered by the inversion with crustal residual in the cratonic cores of North America, Central Europe, Siberia and East Antarctica. In contrast, the inversion with the isostatic residual does not show the cratons. The cratonic mantle keels affect surface topography, and hence are removed by the isostatic correction.

https://doi.org/10.5194/se-2019-203
Preprint. Discussion started: 24 February 2020
© Author(s) 2020. CC BY 4.0 License.


The density of the oceanic mantle is expected to increase with age follow the cooling trend, which also explains sea floor subsidence. The inversion with crustal residual shows some decreased density associated with mid-oceanic ridges, but vote maps are unsuited to resolve the continuous gradient associated with the cooling of the plate. When using the isostatic residual, ocean floor subsidence and the cooling trend has already been accounted for during the isostatic correction and is thus not resolved by the inversion.

Subducted slabs are denser than surrounding mantle immediately after subduction. As the plate sinks, heat diffuses into the plate from the surrounding mantle, so that the plate slowly loses its negative buoyancy. How quickly a subducted plate thermally equilibrates depends on how effecitvely heat is transported to the slab by convection and conduction. Since some slabs seem to stagnate on mantle discontinuities, it is conceivable for a slab to loose all or most of its negative buoyancy. We compared our results with the slab depth contours from Slab 1.0 (Hayes et al., 2012).

Out of the 12 slabs contained in Slab1.0, only five are detected as positive velocity anomalies based on the vote maps (Fig. 8a) and only at depths greater of 200 km or more. These are Izu-Bonin, Kermadec-Tonga, Kamachtka/Kurils/Japan, South America and Sumatra, according to the terminology of Slab1.0.

Th reason might be that the tomography models are too heterogeneous in quality and resolution to resolve these relatively narrow features. Of course, vote maps are not the only way to extract feature from seismic tomographies and an alternative would be to use the 'best' seismic tomography model available instead of a collection of models. But there are no clear criteria which tomography result is the best, except that newer results are probably based on more and better data. Furthermore, there is some evidence that the differences between tomography models partly reflect different regularization parameters, rather than different resolved features (Root et al., 2016), (Root 2019 submitted). Thus, vote maps only extract the feature that are resolved by a majority of tomographic models

Still, out of the five detected slabs, four have positive density contrasts (+5 to +10) in the inversion with the isostatic residual (Fig. 8b). However, these densities are not continuous over the entire depth range of the slabs and are limited to depths between 400 and 700 km. Similar results are obtained using the crustal residual as input, but the densities are more sporadic and concentrated at a single depth of 400 km and have stronger density variations of up to +30 (Fig. 8c).

Based on these results, we think that the density inversion gives acceptable results overall for most of the mantle. The binary classification scheme we use to extract regions from the vote maps leads to a very rough representation in the upper 300 km, which likely contributes to the poor data fit obtained using the crustal residual. In addition, we assume a constant density contrast over the vertical resolution of 100 km. Thus, the volume of relatively thin structures like slabs might be smeared out over a too large depth range.

5.2 Viscosity inversion vs. density inversion

Density inversion is – in a sense – the opposite of viscosity inversion (as done e.g. in Steinberger (2016)). Viscosity inversion assumes that the densities are determined by the velocity to density conversion, whereas density inversion leaves the densities free. Both of these end-members have their merits and drawbacks. Most importantly, velocity-density conversion precludes major compositional variation while density inversion probably underestimates the importance of temperature variations. Nu-

https://doi.org/10.5194/se-2019-203
Preprint. Discussion started: 24 February 2020
© Author(s) 2020. CC BY 4.0 License.

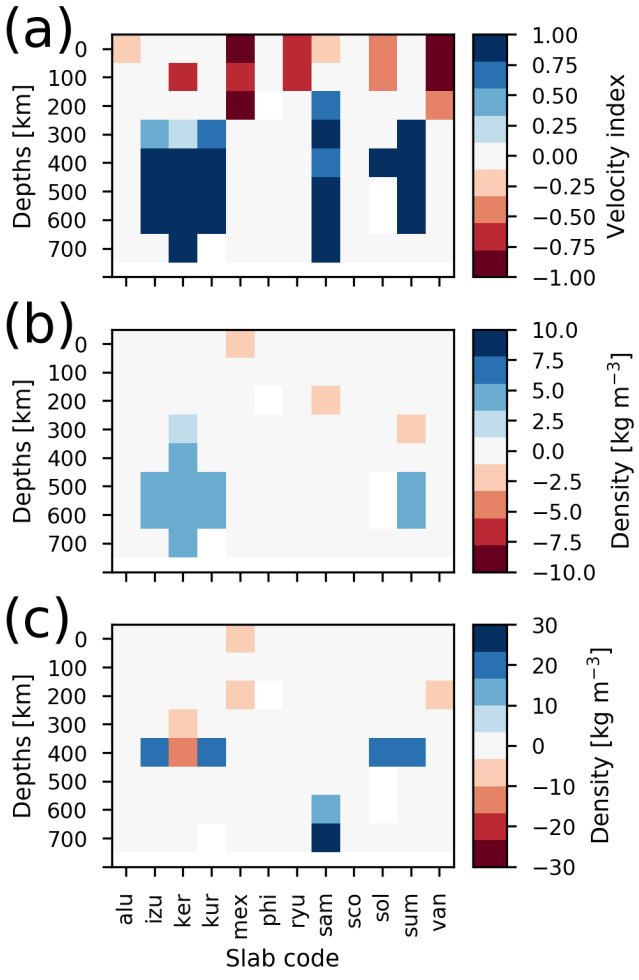

Figure 8. Comparison with Slab1.0 (Hayes et al., 2012). The slab codes stand for: alu - Alaska-Aleutians; izu - Izu-Bonin; ker - Kermadec-Tonga; kur - Kamchatka/Kurils/Japan; mex - Central America; phi - Philippines; ryu - Ryukyu; sam - South America; sco - Scotia; sol - Solomon Islands; sum - Sumatra; van - Santa Cruz Islands /Vanuatu/Loayalty Islands. a) Average value of the velocity anomalies inside the Slab1.0 contour, where 1=positive, -1=negative anomaly. b) Average density value from inversion using the isostatic residual. c) Average density value from inversion of the crustal residual.

https://doi.org/10.5194/se-2019-203
Preprint. Discussion started: 24 February 2020
© Author(s) 2020. CC BY 4.0 License.


merous workers have already introduced additional degrees of freedom to such inversions, (e.g. Steinberger (2016)), but further work is required to properly weigh these two possibilities.

Both techniques share a number of properties: They achieve a similar quality of fit with variance reductions between 60 and 75 % (King, 1995), are affected by non-uniqueness (King and Masters, 1992) and are sensitive to the input seismic data (compare the different viscosity structures presented in King (2016)). Thus, neither of these factors would immediately lead to a preference for a specific technique. However, viscosity inversion is much more parsimonious than density inversion, because a much smaller number of parameters needs to be adjusted to achieve a similar degree of data fit.

The most serious drawback of viscosity inversion is that it leads to unrealistic surface topography, unless the upper mantle is considered carefully (Steinberger, 2016). However, the gravity effect of that surface topography is used to fit the gravity field, even if it is unrealistic. Thus, some form of lithospheric compensation is necessary to reconcile the stresses from the mantle below with observed topography and known crustal structure (Richards and Hager, 1984). By contrast, we think that density inversion leads to a consistent picture for the topography using both the isostatic or crustal residual as input.

If the isostatic residual is used for inversion, the isostatic contribution of the upper mantle density should ideally be zero. After all, these masses should already have been accounted for as part of the isostatic correction. Indeed, the upper mantle contributes less than 250 m to surface topography (Figure 9a). Contrary to expectation, there is negative topographic contribution in continental regions with thick lithosphere (North America, South Africa, Eastern Australia, East Antarctica) due to negative density anomalies in the upper mantle. The likely explanation is that we only use the Moho depth to compensate topography, but in reality there is an additional contribution from the lithospheric mantle. Thus, our isostatic Moho depths is too shallow making the isostatic correction too positive, which is then corrected by the density inversion.

These results are also confirmed by the dynamic topography calculation. With the two-layer viscosity model that we chose, the topography kernels are essentially zero except for the upper 300 km of the mantle. Hence, the predicted dynamic topography is very similar to the isostatic topography. Even at degree 2, where the deviation from isostasy is strongest, there is hardly any topographic contribution, because the high-density LLVPs (the dominating degree 2 structure) are compensated by negative density anomalies above it. This compensation of the LLVPs was also observed in a mantle convection simulation (Liu and Zhong, 2015).

The inversion results with the crustal residual are broadly consistent with this finding, although the poor resolution might hide possible inconsistencies. The isostatic topography contribution of the upper 300 km is considerable (up to 1.5 km) and is mainly negative due to the strong influence of thick lithosphere. In the oceans, only the Pacific spreading ridges are clearly reflected. However, vote maps can only reflect the oceanic cooling trends in a very crude way, such that only the broad ridges in the Pacific can be captured using this technique.

Still, there is qualitative agreement between the residual topography of the crustal model we used and the topography contribution from the upper mantle. This suggests that a more detailed modelling of the mantle lithosphere is sufficient to reduce the magnitude of the gravity anomaly and residual topography. In a recent model (Afonso et al., 2019), we already found that topography and the gravity field can be explained by the upper mantle and topography (above spherical harmonic degree 15),

https://doi.org/10.5194/se-2019-203
Preprint. Discussion started: 24 February 2020
© Author(s) 2020. CC BY 4.0 License.

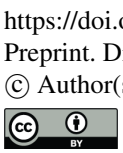

Solid Earth
Discussions
Open Access
EGU

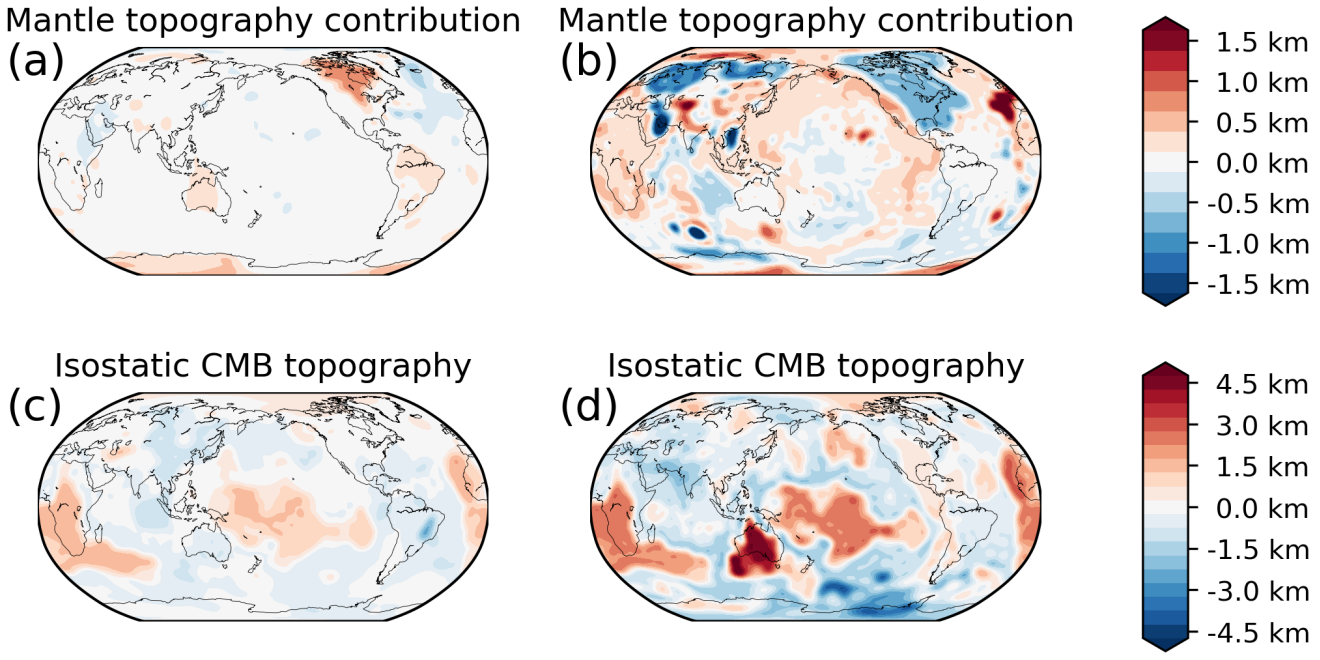

Figure 9. Isostatic contributions to boundary deformations from inverted density model. To facilitate comparison with the dynamic topography in Fig. 10 the results have been filtered to spherical harmonic degree 30. a) Contribution of upper 300 km to surface topography for the inversion results based on the isostatic residual. b) The same for the results based on the crustal residual. c) Contribution of the lower 800 km of the mantle to topography at the core-mantle boundary based on the isostatic residual inversion d) The same for the crustal residual inversion.

while still staying within the uncertainty of the global seismological model Litho1.0 (Pasyanos et al., 2014). The results we present here would agree with this finding on even larger scales.

5.3 Impact of CMB topography

To estimate the impact of CMB topography, we use the results based on the isostatic residual gravity. If the lower 800 km of the mantle are isostatically balanced on the CMB and assuming a density contrast of 4500 $\mathrm{kg\,m^{-3}}$ at the CMB, the inverted density structure would lead to CMB undulations of $\pm 1200\,\mathrm{m}$. At satellite altitude, these undulations would cause a gravity response of $\pm 20\,\mathrm{mGal}$. Due to the great depth of the source, the gravity response is anti-correlated with the proper gravity effect of the density anomalies in the 800 lower km of the mantle. Thus, the gravity effect of CMB deformations would reduce the gravity effect associated with lower mantle density anomalies from $\pm 30\,\mathrm{mGal}$ to $\pm 15\,\mathrm{mGal}$, but do not affect the spatial pattern. Hence, the actual density anomalies in the lower mantle would have to be twice as large to produce the same gravity effect as without CMB deformation.

https://doi.org/10.5194/se-2019-203
Preprint. Discussion started: 24 February 2020
© Author(s) 2020. CC BY 4.0 License.

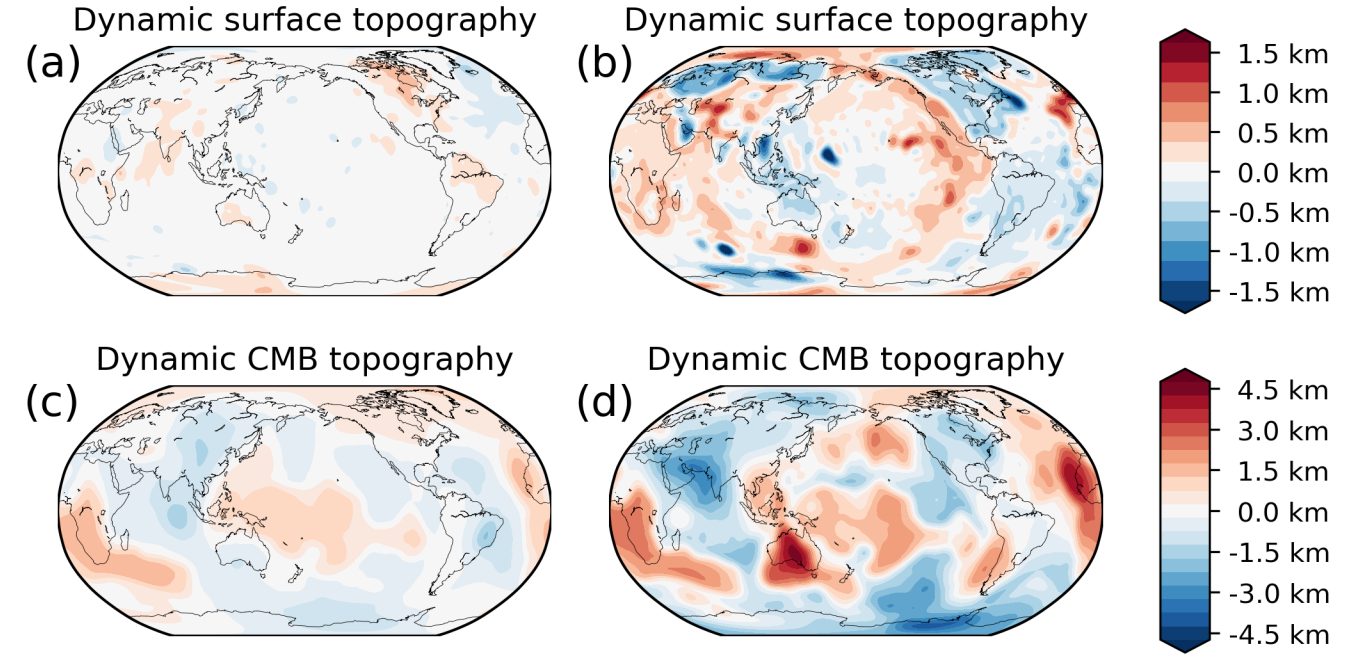

Figure 10. Isostatic contributions to boundary deformations from inverted density model. The results are filtered to spherical harmonic degree 30. a) Contribution of upper 300 km to surface topography for the inversion results based on the isostatic residual. b) The same for the results based on the crustal residual. c) Contribution of the lower 800 km of the mantle to topography at the core-mantle boundary based on the isostatic residual inversion d) The same for the crustal residual inversion.

These results also hold if dynamic topography is used instead of isostatic topography, at least at the wavelengths where the gravity signal of the CMB would be visible (compare Figs. **??**d and 10d).

5.4 Isostatic residual vs. crustal correction

The results obtained with isostatic and crustal residual disagree substantially. The correlation coefficient calculated for individual depth slices is typically less than 0.5, and even negative for some depths. The highest correlations are found in the depth range 2500 - 2800 km and 1500 km - 2000 km and are mainly due to the influence of the LLVPs. In addition, the magnitude of the density anomalies is on average four times larger based on the crustal residual, which agrees with the relative magnitude of the input gravity fields.

Based on the fit to the data, the isostatic residual is preferred, because it achieves both higher absolute and relative data fit. However, the isostatic Moho depths disagree with the seismological determinations. Furthermore, the crustal residual lacks a correction for the oceanic cooling trend, which clearly contributes to the crustal residual. Thus, the better data fit preference for the isostatic residual is not as straightforward.

https://doi.org/10.5194/se-2019-203
Preprint. Discussion started: 24 February 2020
© Author(s) 2020. CC BY 4.0 License.

Solid Earth Discussions

In any case, the isostatic and crustal residual are extreme examples of how the upper Earth can be accounted for in a gravity inversion. Our results clearly demonstrate that these different approaches lead to an enormous spread in terms of the recovered densities in the mantle. At the same time, signals from the deep Earth in terms of gravity or topography might affect modelling of the upper Earth. Commonly, high pass filtering is used to remove the signal of the deep Earth (Bowin, 1991), but this is clearly insufficient, due to the spectral overlap (Root et al., 2015). Thus, a coupled approach that simultaneously considers the entire crust and mantle is required in order to properly model the gravity field and Earth's topography.

5.5 Implications for LLVP temperature and composition

Broadly speaking, the LLVPs could originate from any combination of increased temperature and compositional variation. After their first discovery, the LLVP were initially considered as a purely thermal feature: two "superplumes" that rise from the core-mantle boundary (Dziewonski, 1984). However, even if the LLVPs are purely due to temperature increase, a more likely explanation is that they are swarms of smaller plumes that are smeared due to the limited resolution of seismic tomographies (Schubert et al., 2004; Schuberth et al., 2009), with an additional influence from the stability field of post-Perovskite (Koelemeijer et al., 2018).

In contrast to this isochemical view, some authors have proposed that the LLVPs are chemically distinct from the normal (pyrolitic) mantle. The chemical distinctiveness of the LLVP can either be accumulated over time or be a primitive reservoir that separated early in Earth's history (Deschamps et al., 2012). A likely process for accumulation is the separation of oceanic crust from subducted lithosphere (Mulyukova et al., 2015). If the LLVPs have a compositional component, they have to be intrinsically denser than surrounding pyrolitic mantle to have stayed near the core-mantle boundary, despite very high temperatures. If the LLVPs are indeed an old feature, this would also explain the proposed spatial correlation between plume generation and the edges of the LLVPs over the last 200 million years (Burke et al., 2008).

Our inversion results indicate a positive density anomaly for the LLVPs both using isostatic and crustal residual. This would rule out a purely thermal origin of the LLVPs, since this would lead to negative densities.

In order to test different scenarios using our inversion results, we make use of the petrological data base of Stixrude et al. (Stixrude and Lithgow-Bertelloni (2011)). We construct a simple adiabatic model (see Appendix A) based on a pyrolitic composition for the mantle (Stixrude and Lithgow-Bertelloni, 2012), that serves as reference model. The adiabatic model is entirely self-consistent and the only free parameter is the temperature at the top of the model, which we adjusted in order to fit the surface wave dispersion curves from PREM (Dziewonski and Anderson, 1981). Unlike previous thermochemical interpretations for the lower mantle (e.g. Deschamps et al. (2012)), this corrects for the bias between the petrophysical data base and PREM. Next, we applied first-order perturbations to the model and obtained sensitivities of shear wave velocity and density to changes in temperature, iron content and fraction of Mid-Ocean Ridge Basalt (MORB).

We assume a negative S-wave velocity deviation of 2 per cent for the LLVPs, since most mantle tomographies display roughly this amount of slowness. Our inversion results would place the density anomaly of the LLVP between 0.1 % (isostatic residual) and 0.3 % (crustal residual), but due to possible isostatic compensation at the CMB, (section 5.3), the density anomalies could be twice as large (up to 0.6 %).

https://doi.org/10.5194/se-2019-203
Preprint. Discussion started: 24 February 2020
© Author(s) 2020. CC BY 4.0 License.


A temperature increase of 670 K leads to the required velocity reduction, however it would also entail a density change of -1%, which would be incompatible with our findings. Likewise, a 2.6 % increase of iron content (without temperature change) fits the velocity reduction, but leads to a density increase of 1.6 %. To fit both velocity and our lowest density estimate, a temperature increase of 380 K and an iron increase of 1.1 % is required, while our highest density estimate would require changes of 260 K and 1.6 % FeO respectively.

Adding a MORB fraction leads to higher required temperatures, because MORB is slightly faster than pyrolitic mantle at the depths of the LLVPs, according to our petrophysical calculations. Our lowest density estimate (+0.1 %) would require a temperature change of +870 K and a MORB fraction of 40 % and the highest density estimate (+0.6 %) requires +960 K and 58 % MORB. However, this interpretation is depdendent on the petrological data base of Stixrude et al., which is based on sparse measurements at extremely high pressures. Recent measurements of Calcium-Perovskite (Ca-Pv) (Gréaux et al., 2019; Thomson et al., 2019) imply that seismic velocities in MORB-enriched zones would be lower than thought previously. Thus, less extreme temperatures would be required to reconcile increased density and reduced velocity.

Based on our results it is difficult to express preference for MORB or iron enrichment. Since MORB is introduced to the mantle by subduction, plate reconstructions place some constraints on the amount of MORB produced. Stixrude et al. (Stixrude and Lithgow-Bertelloni (2012)) estimate that the total amount of basalt input into the mantle corresponds to about 10 % of the volume of the mantle. As an absolute upper limit, assuming the LLVPs have a height of 800 km and cover 25 % of the core surface area, the volume would be around 4 % of the total mantle. Thus, to reach a MORB fraction of 60 % in the LLVPs about a fourth of the total generated subducted basalt would need to accumulate.

6 Conclusions

In this paper we have presented how the gravity field and tomographic vote maps can be combined to estimate the density distribution inside the mantle. We have shown that the method is able to reasonably recover expected features in the mantle without requiring any information about the viscosity structure. Still, our recovered density structure leads to qualitative agreement between isostatic and residual topography. Furthermore, our results indicate that the LLVPs are slightly denser and hence chemically distinct.

In our first order analysis, the non-linear dependencies of velocity and density, the impact of melt, heterogeneity inside the LLVPs and the possible presence of post-perovskite is neglected. However, our results can be reconciled with our present knowledge about rock properties at these extreme conditions.

One important difference compared to previous methods is that in our method density is free to vary independent of seismic velocity. While this gives the necessary freedom to the density inversion, it ignores the strong evidence for the important role of temperature. In the future, more precise petrophysical data could help to put constraints on the relative importance of temperature and composition. This would also help to reconcile our results with previous viscosity inversions.

Furthermore, our results show that the lithospheric mantle is critical to resolve disagreements between "bottom-up" and "top-down" methods. In fact, depending on how the lithosphere is treated, the inverted densities can change by a factor of four.

https://doi.org/10.5194/se-2019-203
Preprint. Discussion started: 24 February 2020
© Author(s) 2020. CC BY 4.0 License.


Thus, a combined approach is necessary, where the uncertainties of seismic determinations of the lithosphere are considered in conjunction with signals resulting from deeper density anomalies.

Our inversion breaks down the mantle volume into discrete volumes with a constant density. This reduces the number of unknowns compared to a continuous inversion and means that less regularization is required. However, using vote maps to extract features from a collection of seismic tomographies is the most basic way to do this and a more refined method (e.g. Fadel et al. (2015)) could lead to better constrained volumes. In particular it might benefit an inversion if uncertainties could be placed on the size and position of the volumetric features to allow them to change during inversion.

Instead of relying on seismic tomographies or derived quantities like vote maps, it might be beneficial to stay closer to seismic data. The canonical choice would be seismic travel times and normal modes (as in Dziewonski and Anderson (1981)), but there are more uncommon seismic products that might provide additional constraints. For instance, core-diffracted waves are very sensitive to velocity near the CMB (Hosseini and Sigloch, 2015).

Author contributions. JE developed the initial idea of the project, WS developed the code and ran the calculations. BS benchmarked the topography kernel calculations. WS prepared the manuscript with contributions from JE and BS.

Competing interests. There are no competing interests present.

Code and data availability. All input data of the study are freely available. Gravity data can be downloaded from International Centre for Global Earth Models (ICGEM), vote maps are available from http://www.earth.ox.ac.uk/ smachine, the crustal model is available in supplementary information in Szwillus et al. 2019. Mineos can be downloaded via the Computational Infrastructure for Geodynamics (geodynamics.org/cig/software/mineos), PerpleX is available from the author's website http://www.perplex.ethz.ch/ .

All software required to repeat the calculations presented here will be made available on GitHub before publication.

Acknowledgements. This work was carried out as part of the European Space Agency's Support to Science Element '3D Earth - A dynamic living planet'. The authors thank John Brodholt for his comments on an earlier version of this manuscript.

https://doi.org/10.5194/se-2019-203
Preprint. Discussion started: 24 February 2020
© Author(s) 2020. CC BY 4.0 License.


References

Afonso, J. C., Fullea, J., Griffin, W. L., Yang, Y., Jones, A. G., D. Connolly, J. A., and O'Reilly, S. Y.: 3-D multiobservable probabilistic inversion for the compositional and thermal structure of the lithosphere and upper mantle. I: A priori petrological information and geophysical observables, Journal of Geophysical Research: Solid Earth, 118, 2586–2617, https://doi.org/10.1002/jgrb.50124, 2013.

Afonso, J. C., Salajegheh, F., Szwillus, W., Ebbing, J., and Gaina, C.: A global reference model of the lithosphere and upper mantle from joint inversion and analysis of multiple data sets, Geophysical Journal International, 217, 1602–1628, https://doi.org/10.1093/gji/ggz094, 2019.

Amante, C. and Eakins, B. W.: ETOPO1 Global Relief Model converted to PanMap layer format, https://doi.org/10.1594/PANGAEA.769615.

Ballmer, M. D., Schmerr, N. C., Nakagawa, T., and Ritsema, J.: Compositional mantle layering revealed by slab stagnation at ˜1000-km depth, Science advances, 1, e1500 815, https://doi.org/10.1126/sciadv.1500815., 2015.

Ballmer, M. D., Houser, C., Hernlund, J. W., Wentzcovitch, R. M., and Hirose, K.: Persistence of strong silica-enriched domains in the Earth's lower mantle, Nature Geoscience, 10, 236–240, https://doi.org/10.1038/NGEO2898, 2017.

Bouman, J., Ebbing, J., Meekes, S., Fattah, R. A., Fuchs, M., Gradmann, S., Haagmans, R., Lieb, V., Schmidt, M., Dettmering, D., and Bosch, W.: GOCE gravity gradient data for lithospheric modeling, International Journal of Applied Earth Observation and Geoinformation, https://doi.org/10.1016/j.jag.2013.11.001, http://www.sciencedirect.com/science/article/pii/S0303243413001487, 2013.

Bowin, C.: The Earth's gravity field and plate tectonics, Tectonophysics, 187, 69–89, 1991.

Burke, K., Steinberger, B., Torsvik, T. H., and Smethurst, M. A.: Plume Generation Zones at the margins of Large Low Shear Velocity Provinces on the core–mantle boundary, Earth and Planetary Science Letters, 265, 49–60, https://doi.org/10.1016/j.epsl.2007.09.042, 2008.

Chilès, J.-P. and Delfiner, P.: Geostatistics: Modeling spatial uncertainty, vol. 713 of *Wiley series in probability and statistics*, Wiley, Hoboken, NJ, 2. ed. edn., https://doi.org/10.1002/9781118136188, http://site.ebrary.com/lib/alltitles/docDetail.action?docID=10534032, 2012.

Colli, L., Ghelichkhan, S., and Bunge, H.-P.: On the ratio of dynamic topography and gravity anomalies in a dynamic Earth, Geophysical Research Letters, 43, 2510–2516, https://doi.org/10.1002/2016GL067929, 2016.

Connolly, J. A. D.: The geodynamic equation of state: What and how, Geochemistry, Geophysics, Geosystems, 10, https://doi.org/10.1029/2009GC002540, 2009.

Conrad, C. P., Steinberger, B., and Torsvik, T. H.: Stability of active mantle upwelling revealed by net characteristics of plate tectonics, Nature, 498, 479–482, https://doi.org/10.1038/nature12203, 2013.

Deschamps, F., Cobden, L., and Tackley, P. J.: The primitive nature of large low shear-wave velocity provinces, Earth and Planetary Science Letters, 349-350, 198–208, https://doi.org/10.1016/j.epsl.2012.07.012, 2012.

Dziewonski, A. M.: Mapping the lower mantle: Determination of lateral heterogeneity in P velocity up to degree and order 6, Journal of Geophysical Research: Solid Earth, 89, 5929–5952, https://doi.org/10.1029/JB089iB07p05929, 1984.

Dziewonski, A. M. and Anderson, D. L.: Preliminary reference Earth model, Physics of the Earth and Planetary Interiors, 25, 297–356, https://doi.org/10.1016/0031-9201(81)90046-7, 1981.

Efron, B. and Gong, G.: A leisurely look at the bootstrap, the jackknife, and cross-validation, The American Statistician, 37, 36–48, 1983.

Fadel, I., van der Meijde, M., Kerle, N., and Lauritsen, N.: 3D object-oriented image analysis in 3D geophysical modelling: Analysing the central part of the East African Rift System, International Journal of Applied Earth Observation and Geoinformation, 35, 44–53, https://doi.org/10.1016/j.jag.2013.11.004, 2015.

https://doi.org/10.5194/se-2019-203
Preprint. Discussion started: 24 February 2020
© Author(s) 2020. CC BY 4.0 License.

Flament, N., Gurnis, M., and Müller, R. D.: A review of observations and models of dynamic topography, Lithosphere, 5, 189–210, 2013.

Fullea, J., Afonso, J. C., Connolly, J. A. D., Fernàndez, M., García-Castellanos, D., and Zeyen, H.: LitMod3D: An interactive 3-D software to model the thermal, compositional, density, seismological, and rheological structure of the lithosphere and sublithospheric upper mantle, Geochemistry, Geophysics, Geosystems, 10, n/a–n/a, https://doi.org/10.1029/2009GC002391, 2009.

Garnero, E. J., McNamara, A. K., and Shim, S.-H.: Continent-sized anomalous zones with low seismic velocity at the base of Earth's mantle, Nature Geoscience, 9, 481–489, https://doi.org/10.1038/ngeo2733, 2016.

Griffin, W. L., O'Reilly, S. Y., Afonso, J. C., and Begg, G. C.: The Composition and Evolution of Lithospheric Mantle: A Re-evaluation and its Tectonic Implications, Journal of petrology, 50, 1185–1204, https://doi.org/10.1093/petrology/egn033, 2009.

Gréaux, S., Irifune, T., Higo, Y., Tange, Y., Arimoto, T., Liu, Z., and Yamada, A.: Sound velocity of CaSiO3 perovskite suggests the presence of basaltic crust in the Earth's lower mantle, Nature, 565, 218–221, https://doi.org/10.1038/s41586-018-0816-5, 2019.

Hager, B. H. and O'Connell, R. J.: Kinematic models of large-scale flow in the Earth's mantle, Journal of Geophysical Research, 84, 1031, https://doi.org/10.1029/JB084iB03p01031, 1979.

Hager, B. H., Clayton, R. W., Richards, M. A., Comer, R. P., and Dziewonski, A. M.: Lower mantle heterogeneity, dynamic topography and the geoid, Nature, 313, 541–545, https://doi.org/10.1038/313541a0, 1985.

Hayes, G. P., Wald, D. J., and Johnson, R. L.: Slab1.0: A three-dimensional model of global subduction zone geometries, Journal of Geophysical Research: Solid Earth, 117, n/a–n/a, https://doi.org/10.1029/2011JB008524, 2012.

Hosseini, K. and Sigloch, K.: Multifrequency measurements of core-diffracted P waves (Pdiff) for global waveform tomography, Geophysical Journal International, 203, 506–521, https://doi.org/10.1093/gji/ggv298, 2015.

Hosseini, K., Matthews, K. J., Sigloch, K., Shephard, G. E., Domeier, M., and Tsekhmistrenko, M.: SubMachine: Web-Based Tools for Exploring Seismic Tomography and Other Models of Earth's Deep Interior, Geochemistry, geophysics, geosystems : G(3), 19, 1464–1483, https://doi.org/10.1029/2018GC007431, 2018.

Ishii and Tromp: Normal-mode and free-Air gravity constraints on lateral variations in velocity and density of Earth's mantle, Science (New York, N.Y.), 285, 1231–1236, https://doi.org/10.1126/science.285.5431.1231, 1999.

Jordan, T. H.: Composition and development of the continental tectosphere, Nature, 274, 544–548, https://doi.org/10.1038/274544a0, 1978.

Karato, S.-i.: Importance of anelasticity in the interpretation of seismic tomography, Geophysical Research Letters, 20, 1623–1626, https://doi.org/10.1029/93GL01767, 1993.

King, S. D.: The viscosity structure of the mantle, Reviews of Geophysics, 33, 11, https://doi.org/10.1029/95RG00279, 1995.

King, S. D.: An evolving view of transition zone and midmantle viscosity, Geochemistry, Geophysics, Geosystems, 17, 1234–1237, https://doi.org/10.1002/2016GC006279, 2016.

King, S. D. and Masters, G.: An inversion for radial viscosity structure using seismic tomography, Geophysical Research Letters, 19, 1551–1554, https://doi.org/10.1029/92GL01700, 1992.

Koelemeijer, P., Deuss, A., and Ritsema, J.: Density structure of Earth's lowermost mantle from Stoneley mode splitting observations, Nature communications, 8, 15 241, https://doi.org/10.1038/ncomms15241, 2017.

Koelemeijer, P., Schuberth, B., Davies, D. R., Deuss, A., and Ritsema, J.: Constraints on the presence of post-perovskite in Earth's lowermost mantle from tomographic-geodynamic model comparisons, Earth and Planetary Science Letters, 494, 226–238, https://doi.org/10.1016/j.epsl.2018.04.056, 2018.

Laske, G., Masters, T. G., Ma, Z., and Pasyanos, M. E.: Update on CRUST1.0 - A 1-degree Global Model of Earth's Crust, Geophysical Research Abstracts, 15, https://igppweb.ucsd.edu/~gabi/crust1.html, 2013.

https://doi.org/10.5194/se-2019-203
Preprint. Discussion started: 24 February 2020
© Author(s) 2020. CC BY 4.0 License.


Lau, H. C. P., Mitrovica, J. X., Davis, J. L., Tromp, J., Yang, H.-Y., and Al-Attar, D.: Tidal tomography constrains Earth's deep-mantle buoyancy, Nature, 551, 321–326, https://doi.org/10.1038/nature24452, 2017.

Lekic, V., Cottaar, S., Dziewonski, A., and Romanowicz, B.: Cluster analysis of global lower mantle tomography: A new class of structure and implications for chemical heterogeneity, Earth and Planetary Science Letters, 357-358, 68–77, https://doi.org/10.1016/j.epsl.2012.09.014, 2012.

Liu, X. and Zhong, S.: The long-wavelength geoid from three-dimensional spherical models of thermal and thermochemical mantle convection, Journal of Geophysical Research: Solid Earth, 120, 4572–4596, https://doi.org/10.1002/2015JB012016, 2015.

Masters, G., Woodhouse, J. H., and Freeman, G.: Mineos, https://geodynamics.org/cig/software/mineos/, 2019.

Molnar, P., England, P. C., and Jones, C. H.: Mantle dynamics, isostasy, and the support of high terrain, Journal of Geophysical Research: Solid Earth, 120, 1932–1957, https://doi.org/10.1002/2014jb011724, http://dx.doi.org/10.1002/2014JB011724, 2015.

Moulik, P. and Ekström, G.: The relationships between large-scale variations in shear velocity, density, and compressional velocity in the Earth's mantle, Journal of Geophysical Research: Solid Earth, 121, 2737–2771, https://doi.org/10.1002/2015JB012679, 2016.

Mound, J. E. and Buffett, B. A.: Interannual oscillations in length of day: Implications for the structure of the mantle and core, Journal of Geophysical Research: Solid Earth, 108, 347, https://doi.org/10.1029/2002JB002054, 2003.

Mulyukova, E., Steinberger, B., Dabrowski, M., and Sobolev, S. V.: Survival of LLSVPs for billions of years in a vigorously convecting mantle: Replenishment and destruction of chemical anomaly, Journal of Geophysical Research: Solid Earth, 120, 3824–3847, https://doi.org/10.1002/2014JB011688, 2015.

Pail, R., Goiginger, H., Schuh, W.-D., Höck, E., Brockmann, J. M., Fecher, T., Gruber, T., Mayer-Gürr, T., Kusche, J., Jäggi, A., and Rieser, D.: Combined satellite gravity field model GOCO01S derived from GOCE and GRACE, Geophysical Research Letters, 37, n/a–n/a, https://doi.org/10.1029/2010GL044906, 2010.

Pasyanos, M. E., Masters, T. G., Laske, G., and Ma, Z.: LITHO1.0: An updated crust and lithospheric model of the Earth, Journal of Geophysical Research: Solid Earth, 119, 2153–2173, https://doi.org/10.1002/2013jb010626, http://dx.doi.org/10.1002/2013JB010626, 2014.

Priestly, K. and McKenzie, D.: The thermal structure of the lithosphere from shear wave velocities, Earth and Planetary Science Letters, 244, 285–301, https://doi.org/10.1016/j.epsl.2006.01.008, http://dx.doi.org/10.1016/j.epsl.2006.01.008, 2006.

Ricard, Y., Richards, M., Lithgow-Bertelloni, C., and Le Stunff, Y.: A geodynamic model of mantle density heterogeneity, Journal of Geophysical Research: Solid Earth, 98, 21 895–21 909, https://doi.org/10.1029/93JB02216, 1993.

Richards, M. A. and Hager, B. H.: Geoid anomalies in a dynamic Earth, Journal of Geophysical Research: Solid Earth, 89, 5987–6002, https://doi.org/10.1029/JB089iB07p05987, 1984.

Roberts, P. H. and Aurnou, J. M.: On the theory of core-mantle coupling, Geophysical & Astrophysical Fluid Dynamics, 106, 157–230, https://doi.org/10.1080/03091929.2011.589028, 2012.

Root, B. C., Wal, W., Novák, P., Ebbing, J., and Vermeersen, L. L.: Glacial isostatic adjustment in the static gravity field of Fennoscandia, Journal of Geophysical Research: Solid Earth, 120, 503–518, 2015.

Root, B. C., Ebbing, J., van de rWal, W., England, R. W., and Vermeersen, L.: Comparing gravity-based to seismic-derived lithosphere densities: A case study of the British Isles and surrounding areas, Geophysical Journal International, p. ggw483, https://doi.org/10.1093/gji/ggw483, 2016.

Schaeffer, A. J. and Lebedev, S.: Global Heterogeneity of the Lithosphere and Underlying Mantle: A Seismological Appraisal Based on Multimode Surface-Wave Dispersion Analysis, Shear-Velocity Tomography, and Tectonic Regionalization, in: The Earth's Heterogeneous

https://doi.org/10.5194/se-2019-203
Preprint. Discussion started: 24 February 2020
© Author(s) 2020. CC BY 4.0 License.

Mantle, edited by Khan, A. and Deschamps, F., pp. 3–46, Springer International Publishing, Cham, https://doi.org/10.1007/978-3-319-15627-9_1, 2015.

Schubert, G., Masters, G., Olson, P., and Tackley, P.: Superplumes or plume clusters?, Plumes and Superplumes, 146, 147–162, https://doi.org/10.1016/j.pepi.2003.09.025, 2004.

Schuberth, B. S. A., Bunge, H.-P., Steinle-Neumann, G., Moder, C., and Oeser, J.: Thermal versus elastic heterogeneity in high-resolution mantle circulation models with pyrolite composition: High plume excess temperatures in the lowermost mantle, Geochemistry, Geophysics, Geosystems, 10, n/a–n/a, https://doi.org/10.1029/2008GC002235, 2009.

Shephard, G. E., Matthews, K. J., Hosseini, K., and Domeier, M.: On the consistency of seismically imaged lower mantle slabs, Scientific reports, 7, 10 976, https://doi.org/10.1038/s41598-017-11039-w, 2017.

Steinberger, B.: Effects of latent heat release at phase boundaries on flow in the Earth's mantle, phase boundary topography and dynamic topography at the Earth's surface, Physics of the Earth and Planetary Interiors, 164, 2–20, https://doi.org/10.1016/j.pepi.2007.04.021, 2007.

Steinberger, B.: Topography caused by mantle density variations: Observation-based estimates and models derived from tomography and lithosphere thickness, Geophysical Journal International, 205, 604–621, https://doi.org/10.1093/gji/ggw040, 2016.

Stixrude, L. and Lithgow-Bertelloni, C.: Thermodynamics of mantle minerals - I. Physical properties, Geophysical Journal International, 162, 610–632, https://doi.org/10.1111/j.1365-246X.2005.02642.x, 2005.

Stixrude, L. and Lithgow-Bertelloni, C.: Thermodynamics of mantle minerals - II. Phase equilibria, Geophysical Journal International, 184, 1180–1213, https://doi.org/10.1111/j.1365-246X.2010.04890.x, 2011.

Stixrude, L. and Lithgow-Bertelloni, C.: Geophysics of Chemical Heterogeneity in the Mantle, Annual Review of Earth and Planetary Sciences, 40, 569–595, https://doi.org/10.1146/annurev.earth.36.031207.124244, 2012.

Szwillus, W., Ebbing, J., and Holzrichter, N.: Importance of far-field topographic and isostatic corrections for regional density modelling, Geophysical Journal International, 207, 274–287, https://doi.org/10.1093/gji/ggw270, 2016.

Szwillus, W., Afonso, J. C., Ebbing, J., and Mooney, W. D.: Global Crustal Thickness and Velocity Structure From Geostatistical Analysis of Seismic Data, Journal of Geophysical Research: Solid Earth, 124, 1626–1652, https://doi.org/10.1029/2018JB016593, 2019.

Tanaka, S.: Constraints on the core-mantle boundary topography from P 4 KP-PcP differential travel times, Journal of Geophysical Research, 115, 1063, https://doi.org/10.1029/2009JB006563, 2010.

Thomson, A. R., Crichton, W. A., Brodholt, J. P., Wood, I. G., Siersch, N. C., Muir, J. M. R., Dobson, D. P., and Hunt, S. A.: Seismic velocities of CaSiO3 perovskite can explain LLSVPs in Earth's lower mantle, Nature, 572, 643–647, https://doi.org/10.1038/s41586-019-1483-x, 2019.

van der Meer, D. G., Spakman, W., and van Hinsbergen, D. J.: Atlas of the underworld: Slab remnants in the mantle, their sinking history, and a new outlook on lower mantle viscosity, Tectonophysics, 723, 309–448, https://doi.org/10.1016/j.tecto.2017.10.004, 2018.

van der Meijde, M., Pail, R., Bingham, R., and Floberghagen, R.: GOCE data, models, and applications: A review, International Journal of Applied Earth Observation and Geoinformation, 35, 4–15, https://doi.org/10.1016/j.jag.2013.10.001, 2015.

https://doi.org/10.5194/se-2019-203
Preprint. Discussion started: 24 February 2020
© Author(s) 2020. CC BY 4.0 License.

Solid Earth Discussions

Appendix: Adiabatic model

We derived a simple 1-D adiabatic model of Earth's mantle, based on a petrological data base (Stixrude and Lithgow-Bertelloni, 2005, 2011). We assume a pyrolitic composition (45.1 % SiO2, 38.1 % MgO, 8.0 % FeO, 3.3 % Al2O3, 3.1 % CaO) throughout the entire mantle.

The main relations are as follows: Density $\rho(P,T)$, specific heat capacity $c_p(P,T)$ and heat expansivity $\alpha(P,T)$ are functions of temperature and pressure, and are calculated using the Stixrude data base with PerpleX (Connolly, 2009). Pressure is purely hydrostatic:

$$\frac{\partial P}{\partial r} = -\rho g. \tag{7}$$

The temperature is purely adiabatic, such that

$$\frac{\partial T}{\partial r} = -\frac{T\alpha g}{c_p}. \tag{8}$$

The gravity acceleration at a specific depth is determined by the internal mass at that depth:

$$g(r) = \frac{GM_{int}(r)}{r^2} \tag{9}$$

and the internal mass is decreasing with depth according to:

$$\frac{\partial M_{int}}{\partial r} = +4\pi r^2 \rho \tag{10}$$

This set of equations can be solved by finite differences if the pressure, temperature and gravity strength are specified at the top of the model domain. First, the ρ, c_p and α belonging to these $P-T$ conditions are calculated using PerpleX (Connolly, 2009). Then, these values are used to update pressure, temperature and internal mass:

$$\begin{aligned} P(r-\Delta r) &= P(r) + \rho(r) g(r) \Delta r \\ T(r-\Delta r) &= T(r) + \frac{T(r)\alpha(r) g(r)}{c_p(r)} \Delta r \\ M_{int}(r-\Delta r) &= M_{int}(r) - 4\pi r^2 \rho(r) \Delta r \end{aligned} \tag{11}$$

This process is repeated iteratively from the top of the model domain down to the core-mantle boundary, with a step size Δr of 1 km.

We begin this integration at a depth of 80 km, with a pressure of 2.5 GPa and $g = 9.81 \frac{m}{s^2}$. In order to determine the temperature at the top, we relied on the PREM (Dziewonski and Anderson, 1981). At first we attempted to directly minimize the

https://doi.org/10.5194/se-2019-203
Preprint. Discussion started: 24 February 2020
© Author(s) 2020. CC BY 4.0 License.

Solid Earth Discussions

difference between the velocities in the PREM and the modelled velocity from PerpleX. However, this approach was unsuccessful, because the depths of the main discontinuities in PREM (410 km, 660 km) are incompatible with the Stixrude data base.

Instead, we relied on Rayleigh wave dispersion curves to choose the temperature at the top of the model. Using MineOS (Masters et al., 2019) we calculated the phase velocity of the fundamental Rayleigh wave between frequencies of 0 and 50 mHz for the PREM and for the adiabatic model, for temperatures at the top between 1300 and 1800 K in steps of 50 K. We found that a top temperature of 1550 K gives the best fit to the PREM dispersion curves (Fig. 11a), if equal weight is given to phase velocities at all periods. In particular, we find that the $T = 1550\,K$ model fits the dispersion curve data with an average relative accuracy of 0.3 %, which is similar to the fit that the PREM fits the data used in its construction. Thus, our model is equivalent to the PREM with respect to the dispersion curve data. During these calculations we also found that the presence of post-perovskite phase completely prevents fitting the long-period dispersion curves, so we excluded post-perovskite from the PerpleX calculations.

The resulting temperature curve for the preferred model is nearly linear, but shows a distinct kink below the 660 km discontinuity, due to the different properties of perovskite and a slower temperature increase at greater depths due to the decrease of thermal expansivity α (Fig. 11b). The temperature at the bottom of the mantle is roughly 2350 K. The pressure curve is also nearly linear, but is slightly bent due to the increase of density with depth.

We then applied first order perturbations in terms of temperature, iron content and Mid Oceanic Ridge Basalt (MORB) fraction to the adiabatic model. The vertical resolution of our density models is 100 km, so we applied the perturbation over the same depth range. To determine the sensitivity to temperature variations, we simply used our existing lookup table from PerpleX, while for compositional variations we determined new phase equilibria and corresponding rock properties with FeO content increased by 1%. For the MORB we proceeded somewhat differently, because the MORB is likely not in phase equilbrium with the surrounding mantle rocks, due to the long timescale of chemical diffusion (Stixrude and Lithgow-Bertelloni, 2012). Thus, we determined the phase equilibrium of a pure MORB and then calculated velocities and densities as volume averages of the MORB fraction and the surrounding mantle. These results can be used together to determine how sensitive v_s and density are to changes in temperature, iron content or MORB fraction (Fig. 12)

https://doi.org/10.5194/se-2019-203
Preprint. Discussion started: 24 February 2020
© Author(s) 2020. CC BY 4.0 License.

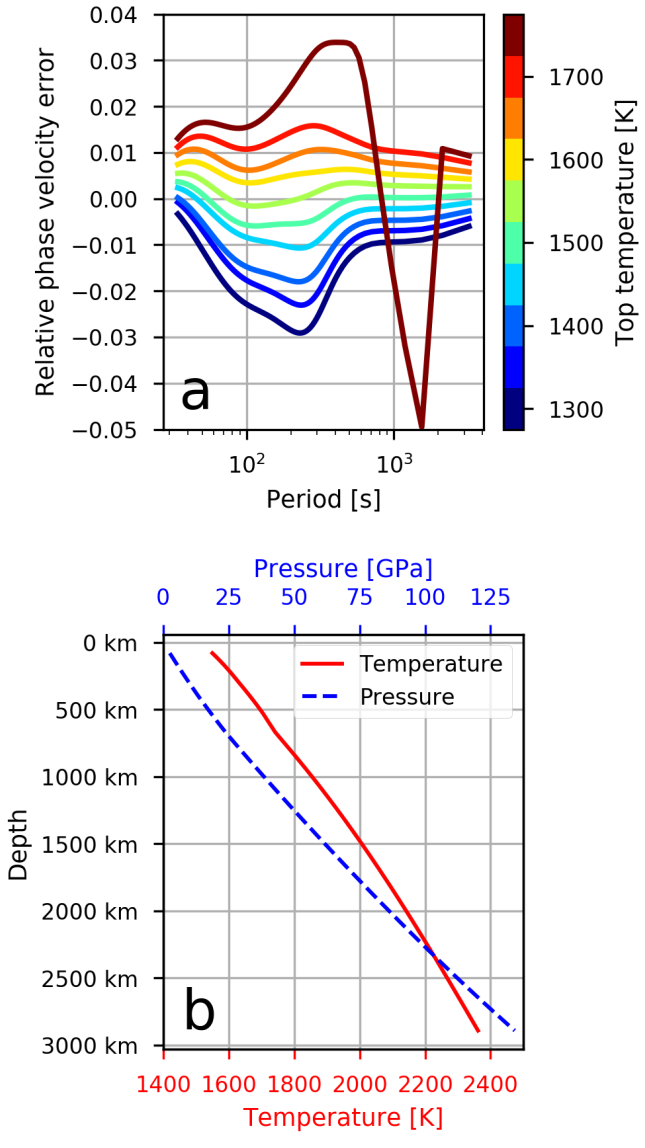

Figure 11. Results of the adiabatic model. a) Raleigh wave phase velocity error relative to PREM for different temperatures at the top of the adiabatic model (80 km). b) Temperature and pressure profiles for the preferred model with $T_{top} = 1550\,\mathrm{K}$

https://doi.org/10.5194/se-2019-203
Preprint. Discussion started: 24 February 2020
© Author(s) 2020. CC BY 4.0 License.

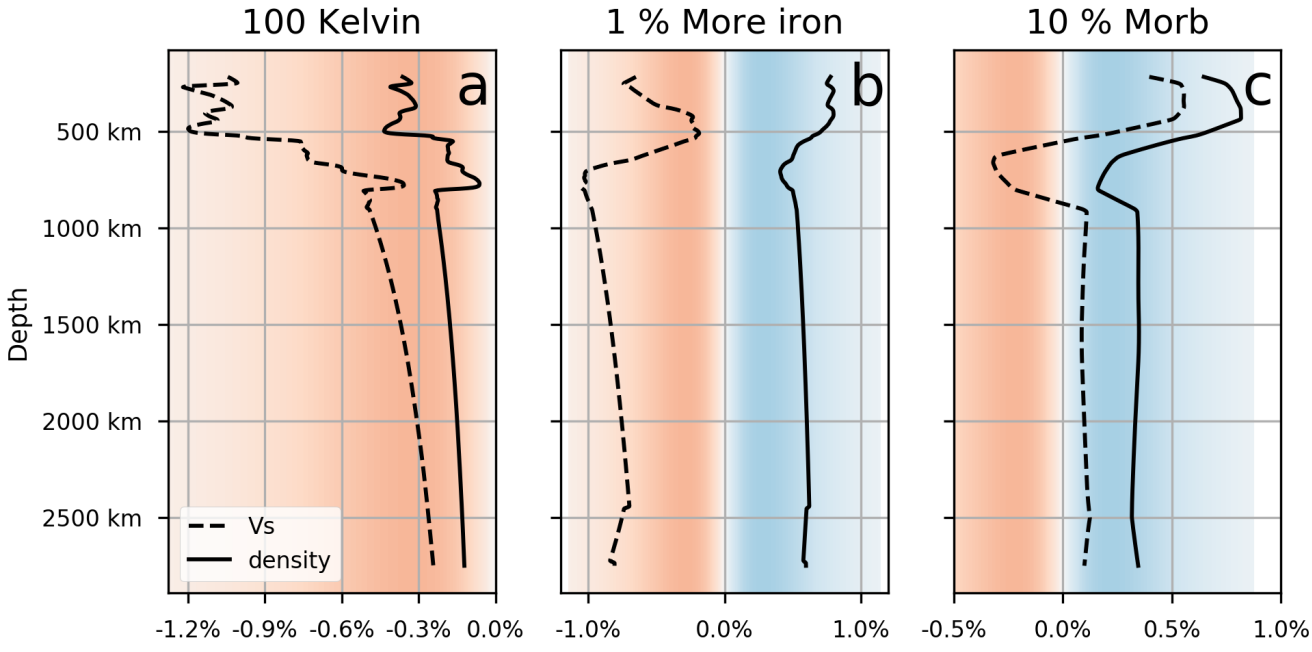

Figure 12. First order perturbation curves for deviations from a adiabatic, hydrostatic model with pyrolitic composition. The red and blue background shading indicates negative and positive changes of the respective quantity. a) Relative change for a temperature change of 100 K. b) Relative change for including 1 % more FeO. c) Relative change for a mixture of 90 % pyrolite and 10% MORB.